Materials Science Forum
ISSN: 1662-9752, Vol. 1184, pp 21-33
doi:10.4028/p-9iISdK

Submitted: 2026-01-15
Revised: 2026-02-16
Accepted: 2026-02-21
Online: 2026-04-14

Multiscale Simulation of Asperity Flattening with Realistic Surface Topography and Microstructure

Aiden Carley-Clopton[1,a*], Grethe Winther[1,b], Javad Hazrati[2,c] and Chris Valentin Nielsen[1,d]

[1]Department of Civil and Mechanical Engineering, Technical University of Denmark, Kongens Lyngby, Denmark

[2]Nonlinear Solid Mechanics, Faculty of Engineering Technology, University of Twente, Enschede, The Netherlands

[a*]aidca@dtu.dk, [b]grwi@dtu.dk, [c]j.hazratimarangalou@utwente.nl, [d]cvni@dtu.dk

[*]corresponding author

Keywords: multiscale simulation, crystal plasticity, asperity flattening.

Abstract. In metal forming, the flattening of asperities on the workpiece surface is important to understand both for the impact it has on the properties of finished parts and the influence that real contact area has on tribological conditions during forming. The current study presents a method for the numerical modeling of asperity flattening of a deep drawing steel under high normal loads and no subsurface strain. At the microscale, a crystal plasticity model is employed to capture the propensity of grains to deform differently depending on their orientation. The continuum scale model is used to provide the boundary conditions to the microscale. The mechanical and microstructural properties of a DC04 deep drawing steel are used to provide the necessary parameters for the continuum and microscale models. The initial surface topography of the experimental material is measured by confocal microscopy and is mimicked in the input to the simulations. Surface topography measurements after flattening the experimental surface are used as validation for the simulated results, with real contact area, mean surface roughness, and autocorrelation length used as the primary figures of merit.

Introduction

When developing a metal forming process, it is important to consider the effect of friction between the tool and workpiece. There are many different modeling frameworks for describing the relationship between the applied normal pressure and the resulting friction in an interface. An early approach which is still widely used is the Amontons-Coulomb model proposing a linear relationship between the nominal contact pressure and the friction stress, related by the friction coefficient μ. For higher normal pressures, another model was proposed by Orowan [1] with a change from linear friction governed by μ to constant friction where the friction stress stops increasing once the material shear flow stress is reached. Early experiments found that the transition between these two regimes is gradual rather than abrupt [2,3]. This phenomenon can be explained by the development of real contact area with contact pressure. Because contact between surfaces is governed by the interaction of neighboring asperities, the real contact area is often much smaller than the apparent contact area. Real contact area is often described by the contact area ratio, α, which is the proportion of the real area of contact to the apparent contact area. Wanheim et al. [4] described this relationship with the follow equation:

$$\tau = f\alpha k \tag{1}$$

where τ is the shear stress from friction, f is a friction factor related to the interface strength, α is the real contact area ratio, and k is the shear flow stress of the material. To model friction behavior using this formulation, it is then necessary to describe how the contact area ratio evolves throughout a process. One way to do so is to consider geometrically uniform model asperities. Previous work in the literature has modeled flattening of model asperities analytically [3-5] and via finite element

modeling (FEM) [6-8]. When using FEM, it is also possible to model flattening using more realistic surface topographies [9,10], which can be beneficial as the transfer of quantitative findings from model to real asperity behavior can be limited [11].
While metallic materials are usually modelled as a continuum, it is important to consider the inhomogeneity of the material at the grain scale when studying effects that result from neighboring grains deforming differently, such as surface roughening. In forming operations, there is a balance of flattening from contact and roughening from nonhomogeneous deformation at the micro-scale, and depending on the forming parameters and material properties, the roughness of metal surfaces either increase or decrease during forming [12]. To examine this phenomenon, FEM studies have been conducted to take into account the effect of grain-scale deformation on roughening considering grain size effects [13], the formation of specific surface morphologies [14], the effect of roughening from pre-straining on subsequent friction behavior [15], and the effect of roughening on formability [16]. It has also been found that roughening from pre-straining can have an impact on the friction coefficient between metal sheet and a tool [17]. The aim of the present study is to use simulation of upsetting tests with a high diameter to height ratio as a benchmark to validate the combination of modelling surface flattening from contact and the microscale deformation of individual grains. This is a step towards developing a method which can be used to predict surface behavior in cases where there is both subsurface strain and contact pressure. To compliment the previously mentioned studies modeling roughening at high subsurface strains in the absence of surface flattening, this paper examines the compression of a thin disk with primary focus on high contact pressure with relatively low subsurface strain.

Experimental Methods

This section covers the methods employed to gather the experimental results presented in this study. The material for all experiments was 0.7 mm thick sheet of DC04 deep drawing steel laser cut into 11 mm rounds. To remove prior lubricant, specimens were cleaned in ethanol in an ultrasonic bath for 5 minutes.

Surface Compression Testing.

Round sheet specimens with an 11 mm diameter were compressed in the setup shown in Figure 1. Specimens were sandwiched between sapphire die buttons with an Sa value less than 0.05 µm. A subpress with spring-return was used for alignment and actuation provided by a servomechanical press with a maximum capacity of 155 kN. The crosshead was moved at a rate of 0.1 mm per second and the test stopped after a maximum load was reached, which after subtraction of the subpress spring forces was equal to that required to achieve the target nominal contact pressure. Five replicates were tested for each nominal pressure.
Mean radial strain was calculated by measuring the specimen diameter with a caliper before and after deformation. Three measurements were taken of each specimen for the undeformed and deformed conditions and the average values used to calculate the mean radial strain.

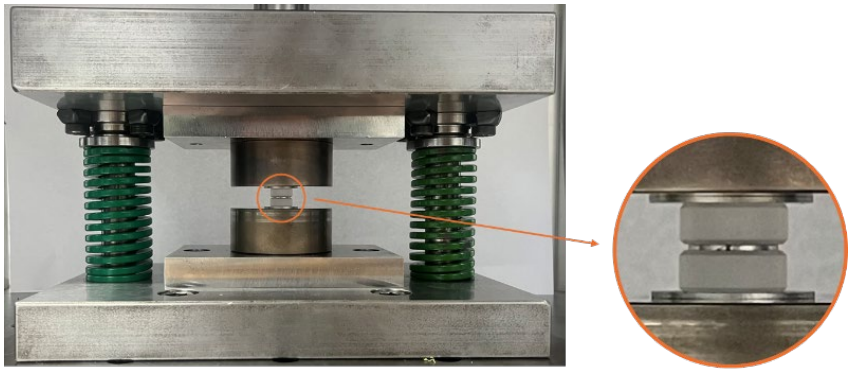

Fig. 1. Compression testing between two sapphire tools in a subpress.

Surface Measurements.

To characterize the contact conditions of the experiments, surface height measurements were taken using a Sensofar S Neox confocal microscope [18]. Scans were taken using a 20x objective lens stitched in a 4x5 grid. Stitching was done with 30 % overlap and a global minimum and maximum focal height shared across all tiles. Each sample was examined in two places on opposite sides of the center line, the same distance from the center of the disk as the area where surface flattening simulation was conducted. Confocal images were leveled and form corrected by subtraction of a second order polynomial fit and filtered with a median filter with a 3x3 kernel to remove points of noise in the surface scan [19].

Contact Area Ratio Approximation.

One way to estimate the real area of contact in cases where it cannot be measured directly is to use the change of the height distribution with asperity flattening. The assumption is that the mode height in the distribution represents the height to which the sample surface was compressed by the tool, and all points above the mode correspond to the elastic spring-back of the surface upon unloading [19]. Following this assumption, the portion of the points at and above the mode height would correspond to the proportion of the surface which had been in contact with the tool and therefore yield the contact area ratio. This assumption is not always accurate, and, while it can be used for comparative purposes, can result in an underestimation of contact area. Furthermore, when creating a surface height distribution from discrete data, it is necessary to create bins to determine probability densities. Since the width of these bins can have a bearing on the results, which can in some cases be a significant limitation, several bin counts were used for comparison as well as evaluation of the robustness of this method.

Microstructure Characterization.

To accurately represent the microstructure in numerical simulations, the size, morphology, and orientation of the grains were characterized. This characterization was accomplished using electron backscatter diffraction (EBSD). Specimens were prepared to examine both the plane containing the rolling direction (RD) and transverse direction (TD), and the plane containing the normal direction (ND) and RD. Specimens were polished with abrasive paper up to P4000 and then electropolished using a Struers LectoPol-5 with a voltage of 31 V, a polishing time of 10 s, and flow setting 10. The EBSD was conducted using a Zeiss Sigma 300 scanning electron microscope with a step size of 2 μm. Grain data was analyzed using AZtecCrystal software.

Tensile Testing.

Tensile testing was performed in order to calibrate the material parameters used in simulations. Testing was performed using the servomechanical press mentioned above at a rate of 0.125 mm/s to achieve quasi-static conditions. Full size type H tensile specimens were used and made according to ISO 6892-1:2019 [20]. Testing was conducted in the rolling direction for five replicates.

Numerical Modeling Methods

Tessellation with Neper.

Grain morphology and crystallographic texture in the surface flattening simulation was represented with a tessellation created using Neper [21], version 3.30. Neper is a software tool which facilitates the generation of polycrystal tessellations and meshes for use in finite element simulations. The grain size and crystallographic texture were taken from the EBSD data. The grain size target was a lognormal distribution with a mean equivalent diameter of 16 μm with a standard deviation of 10 μm. Texture was provided by finding the Euler angles for the centroid of each grain in the EBSD scan, making a randomly ordered list of these values the same length as the number of grains in the tessellation, and providing the Euler angles directly to Neper. A hexahedral mesh was used since hexahedral elements have been found to more accurately represent surface deformation of

polycrystals than tetrahedral elements [22]. The mesh was created using a relative cell length of 2 in Neper's settings, which has been found to deliver adequate results in the simulation of surface roughening [23].

Crystal Plasticity Modeling with DAMASK.

Through DAMASK 2.0.2 [24], a phenomenological crystal plasticity model was employed to simulate the behavior of different grains in the tessellation. Only slip has been considered for this study, so twinning parameters are omitted. The evolution of the shear rate for each slip system, $\dot{\gamma}^{\alpha}$, is described in Eq. 2, where it depends on the reference shear rate $\dot{\gamma}_0^{\alpha}$, resolved shear stress τ^{α}, and slip resistance ξ^{α}. Hardening is described by Eq. 3, where $\dot{\xi}^{\alpha}$ is determined by the slip-slip interaction coefficient h_0^{S-S} and by contributions from each other slip system α' by the ratio of the current slip resistance $\xi^{\alpha'}$ and saturation slip resistance $\xi_{\infty}^{\alpha'}$, the shear rate of that system $\dot{\gamma}^{\alpha'}$, and the slip-slip interaction parameter for the two slip systems $h^{\alpha\alpha'}$.

$$\dot{\gamma}^{\alpha} = \dot{\gamma}_0^{\alpha} \left|\frac{\tau^{\alpha}}{\xi^{\alpha}}\right|^{n} sgn(\tau^{\alpha}) \tag{2}$$

$$\dot{\xi}^{\alpha} = h_0^{S-S} \cdot \sum_{\alpha'=1}^{N_S} \left|\dot{\gamma}^{\alpha'}\right| \left|1 - \frac{\xi^{\alpha'}}{\xi_{\infty}^{\alpha'}}\right| \operatorname{sgn}\left(1 - \frac{\xi^{\alpha'}}{\xi_{\infty}^{\alpha'}}\right) h^{\alpha\alpha'} \tag{3}$$

In order to tune these parameters, a simulated tensile test of a 0.1 mm cube with 219 grains was employed where a polycrystal with texture, grain size, and morphology derived from EBSD results was deformed in uniaxial tension, and stress strain curves created and compared to measurements from tensile testing of real specimens. The final stress-strain behavior of the simulated microstructure is shown in Figure 2. The parameters which were chosen to achieve this calibration are shown in Table 1, along with literature values [24] for the elastic parameters C_{11}, C_{12}, and C_{44}.

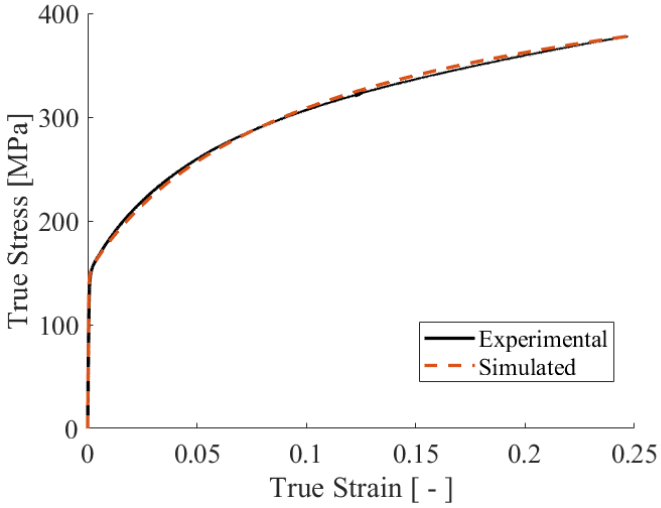

Fig. 2. Representative stress-strain curve for tensile testing of a DC04 deep drawing steel with loading in the rolling direction alongside results of a simulated tensile test of a polycrystal tessellation.

Table 1. Calibrated values for crystal plasticity model.

Parameter	Value Used
ξ_0	88 MPa
ξ_{∞}	205 MPa
h_0^{S-S}	495 MPa
$h^{\alpha\alpha'}$, coplanar	1
$h^{\alpha\alpha'}$, non-coplanar	1.4
C_{11}, C_{12}, C_{44}	233, 135, 118 GPa

Multiscale Modeling.

To limit the number of grains which needed to be simulated, a multiscale approach was applied with a main model and a submodel. The main model is shown in Figure 3 (a), where one eighth of the specimen has been modeled along with the punch, making use of symmetry boundary conditions. Here, no asperities were modeled, and penalty friction was employed with a coefficient μ = 0.08, which has been found in a study of the dry friction of sapphire on steel sheet [25]. Penalty friction is used because the surface is modeled without asperities, meaning that the contact area of the model corresponds to the nominal contact area rather than the real contact area. The current study uses a single value for the friction coefficient for simplicity; however, it would be possible to expand this approach by adding pressure and strain dependency to the friction coefficient based on the micro-scale response. The tool is an analytical rigid body, constrained in the X and Z directions, with a load applied in the -Y direction to develop the desired pressure.

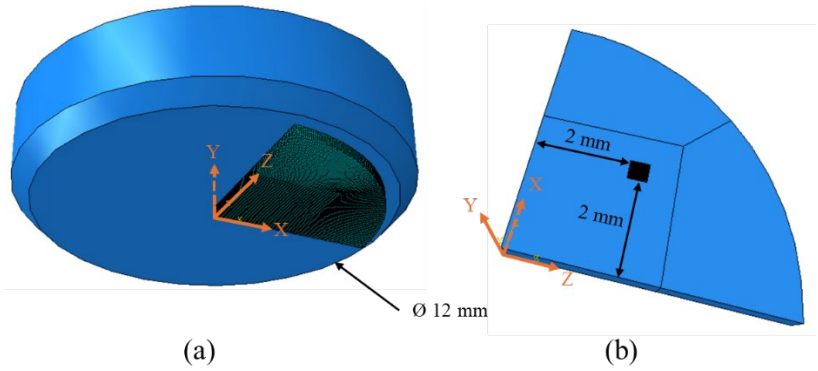

Fig. 3. Simulation setup showing (a) the main model of compression test of a disk with a cylindrical tool and (b) submodel location within the main model. The -X, -Y, and -Z faces of the specimen have symmetry boundary conditions, and the tool is constrained in X and Z with a load applied in the -Y direction.

The polycrystal tessellation was a separate model and was sized at 0.5 x 0.5 x 0.25 mm. An example tessellation can be seen in comparison to an EBSD scan in Figure 4. The polycrystal was given sub-model boundary conditions corresponding to the nodal displacements of a part of the main model 2 mm from the center in both X and Z, as shown in Figure 3 (b). Surface topography was taken directly from down-sampled images of the as-received sheet surface and superimposed onto the top layer of nodes in the model, after which a volumetric smoothing algorithm was applied. Contact at the micro scale was modeled with an analytical rigid tool with a load appropriate to the location of the submodel with respect to the sample center.

A constant shear stress, independent of local contact pressure, was used instead of penalty friction for the microscale model. This was done because the inclusion of asperity topography means that the contact area in the microscale model corresponds to the real area of contact instead of the nominal contact area. The assumption is then made that increase in contact area is the driving mechanism of friction at this scale. This is in line with the approach in previous studies where the dependence of friction stress on normal pressure is described via the increase in contact area with pressure [4]. In this sense, the apparent global friction stress τ can be calculated as:

$$\tau = \tau_i \alpha \tag{4}$$

where τ_i (analogous *fk* in Eq. 1) is the shear stress supported by the interface and α is the contact area ratio. For the main model, the global friction stress is set by:

$$\tau = \mu p \tag{5}$$

where p is the pressure at the contact interface, in this case at the location of the submodel, and the global μ value of 0.08 is used. Using these equations, it is possible to recalculate the appropriate value for τ_i after a simulation based on the plot of α versus p, taking advantage of the near-constant ratio

of α/p for lower pressures. This process was repeated until the value of τ_i converged on 51 MPa, which was used for the subsequent simulations.

Results and Discussion

Contact Pressure Distribution.

Due to the presence of friction, the contact pressure distribution between the tool and sample surfaces is not uniform. It is important to distinguish between the local contact pressure, and the nominal contact pressure p_{nom} which can be defined as:

$$p_{nom} = \frac{F}{A_0} \tag{6}$$

where F is the force applied to the tool and A_0 is the initial, nominal contact area. A plot of local pressure as a function of radial distance from the specimen center is shown in Figure 5. As the applied force increases, the effect of friction on the pressure distribution increases. At higher nominal pressures, a small dip in the local pressure in the center of the specimen appears. This corresponds to the formation of a small dead zone, which has been demonstrated to cause such a pressure drop [26].

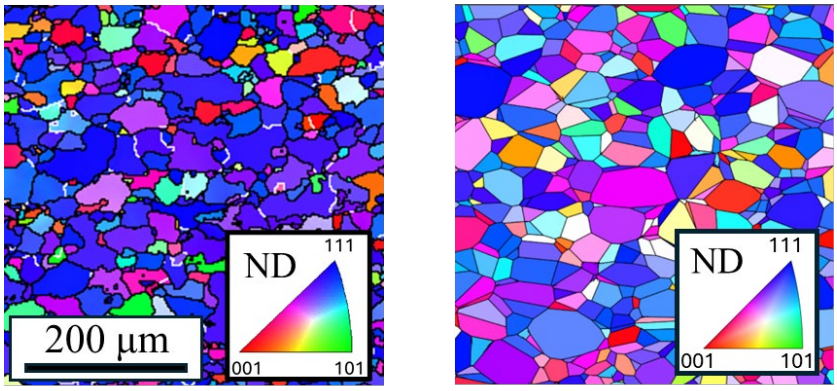

Fig. 4. Comparison of (a) EBSD grain map with (b) tessellation from Neper.

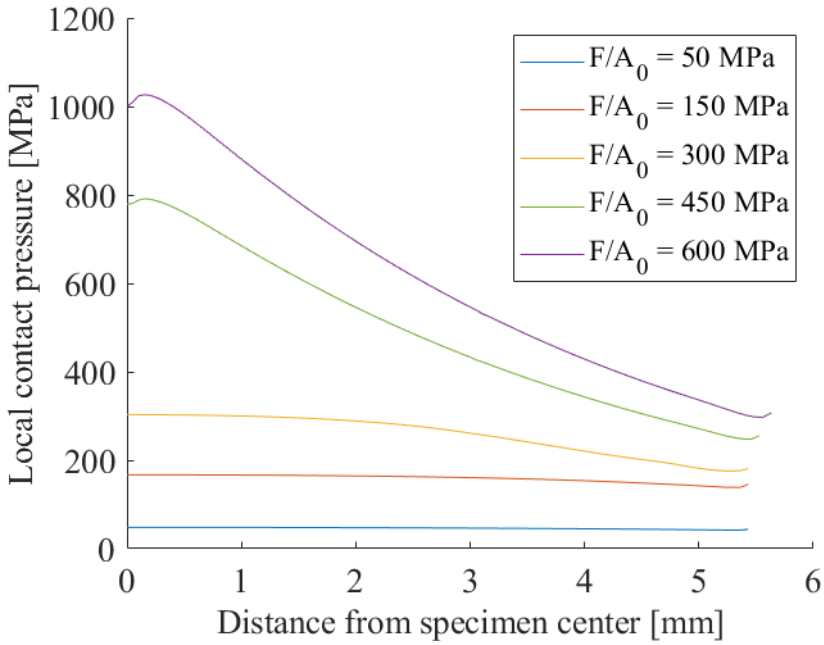

Fig. 5. Local contact pressure as a function of distance from specimen center for different nominal punch pressures for finite element simulation of compression testing of an 11 mm DC04 steel disk (continuum material properties).

Mean Radial Strain Measurements.

The measured mean radial strain for different nominal contact pressure values for both the experimental and simulated compression testing is shown in Figure 6. There is generally good agreement between the two, suggesting that the bulk friction coefficient of 0.08 and the chosen mechanical properties for the continuum model are appropriate. For both the simulation and experiments, there is a sharp increase in the amount of radial strain beginning with 300 MPa nominal pressure. This turn is significant because subsurface strain accelerates the flattening of surface asperities experiments and models [4,25].

Height Maps of Simulated Surface Flattening.

Height maps of surface flattening of a simulated polycrystal are shown in Figure 7. Between 50 MPa and 150 MPa, there is a growth of the contact patches at the tops of asperities, and a joining of nearby areas in contact. With the increase to 300 MPa, there is a sudden shift in the surface, with the contacting areas becoming continuous and the areas not in contact becoming isolated valleys. These valleys shrink further with increased pressure until they are almost entirely gone at 600 MPa. This dramatic change between 150 and 300 MPa reflects the change in the relationship between contact pressure and subsurface strain shown in Figure 6.

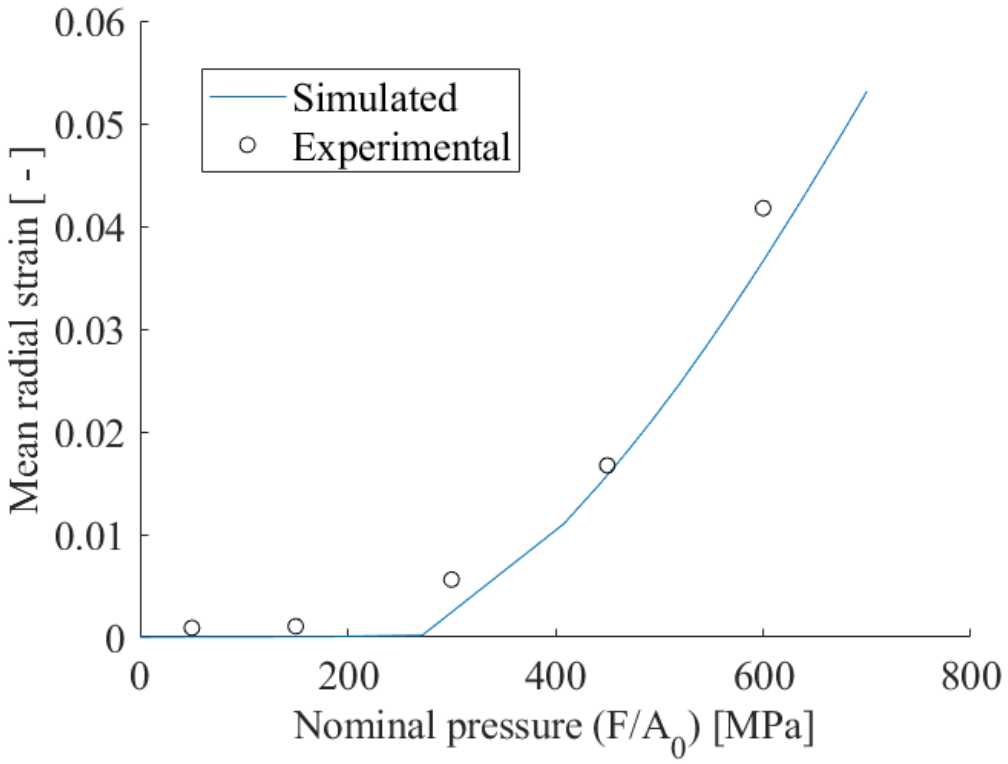

Fig. 6. Mean radial strain as a function of nominal punch pressure for experimental and finite element simulation (with continuum material properties) of the compression of 11 mm DC04 steel disk specimens.

Representative height maps of DC04 specimens subjected to different nominal contact pressures are shown in Figure 8. While the overall trend is similar, with a marked shift between 150 and 300 MPa, there are some differences as well. In comparison to the simulated case, there generally is less flattening apparent in the experimental results, though due to the variability between specimens and locations on specimens, it is difficult to make this comparison quantitatively from height maps alone. Qualitatively, the simulation effectively captures the general character of the flattening response of the surface, as well as the significance of the onset of bulk strain for surface flattening, with perhaps less flattening in the experimental surfaces.

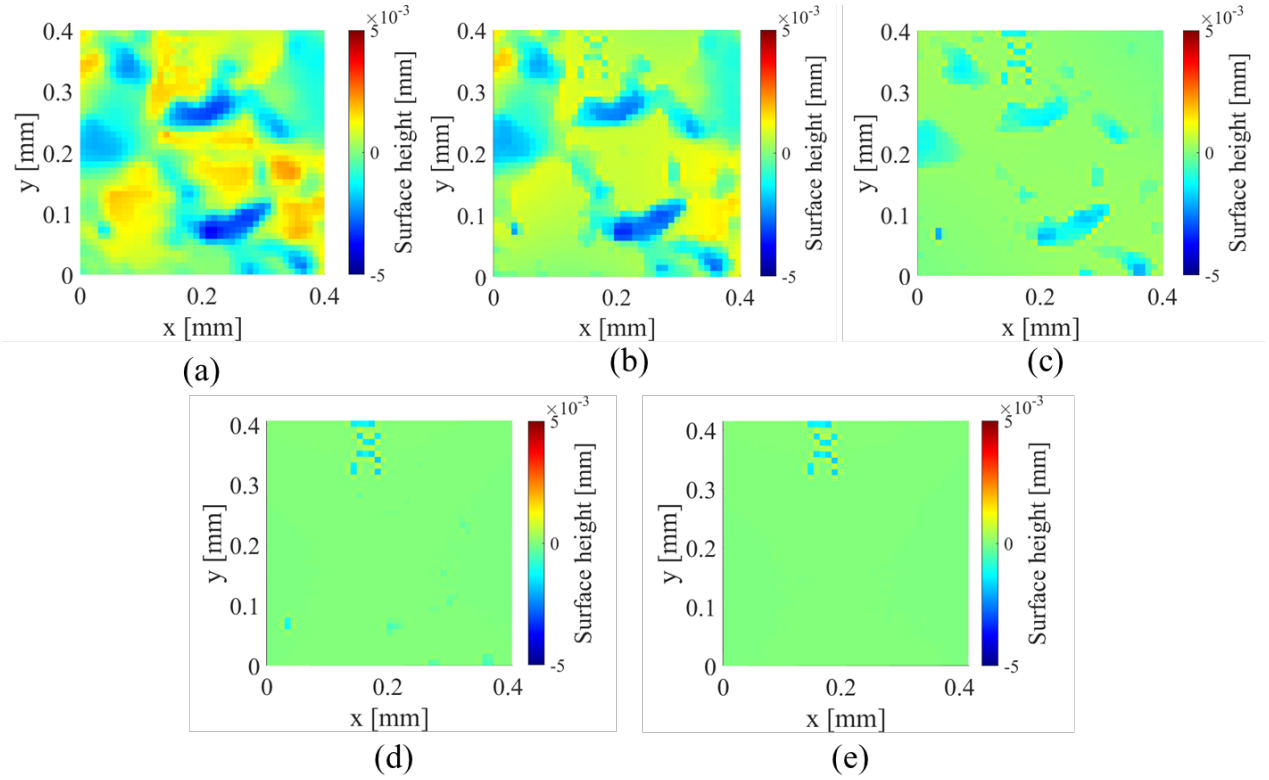

Fig. 7. Height maps of a simulated polycrystal subjected to flattening with a nominal pressure of (a) 50 MPa, (b) 150 MPa, (c) 300 MPa, (d) 450 MPa, and (e) 600 MPa. Strain is applied based on the values taken from a location at a radius of 2.828 mm from the center of an 11 mm disk being compressed between rigid tools.

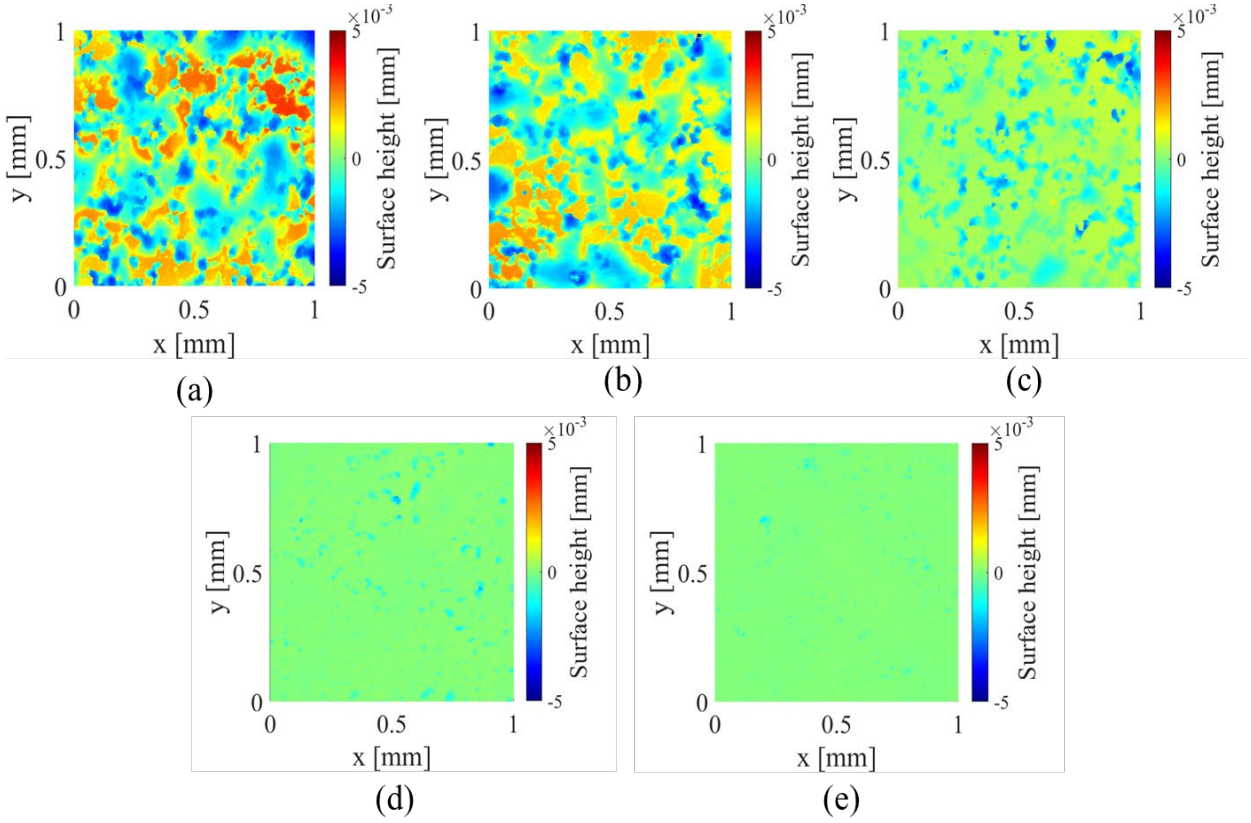

Fig. 8. Surface height scans taken via confocal microscopy of 11 mm DC04 steel disk specimens subjected to compression to nominal contact pressures of (a) 50 MPa, (b) 150 MPa, (c) 300 MPa, (d) 450 MPa, and (e) 600 MPa.

Surface Height Distributions.

Surface height distributions are shown for all the experimental replicates for each nominal pressure along with the relevant simulation results in Figure 9. In general, there is a clear increase in the mode probability density and the formation of a sharp peak as the surface is flattened. This effect is more pronounced for the simulated surface than for the experimental results. There are several possible reasons for this. One is that the simulated surface has a tool which is analytically flat and parallel to the vertical axis of the surface, meaning that all the contact points will have very similar height values. Meanwhile, the real surfaces can have deviations from flat and parallel due to non-uniformities in the sample. While leveling and form removal can compensate for some of this, any tilting of the sample would lead to a broadening of the peak, potentially quite significantly. Another possible explanation is the effect that removing the load from the surface might have on the height distribution for that surface, since the real specimens are unloaded before measurement, while the simulated surface is not. When the flat contact surface elastically relaxes during unloading, some of the points previously in contact will be above the new mode height, and some will be below, thus broadening the peak. Finally, the simulated surfaces are created by down sampling real surface scans, significantly reducing the number of points in surface. This likely has an impact on the resulting height distribution.

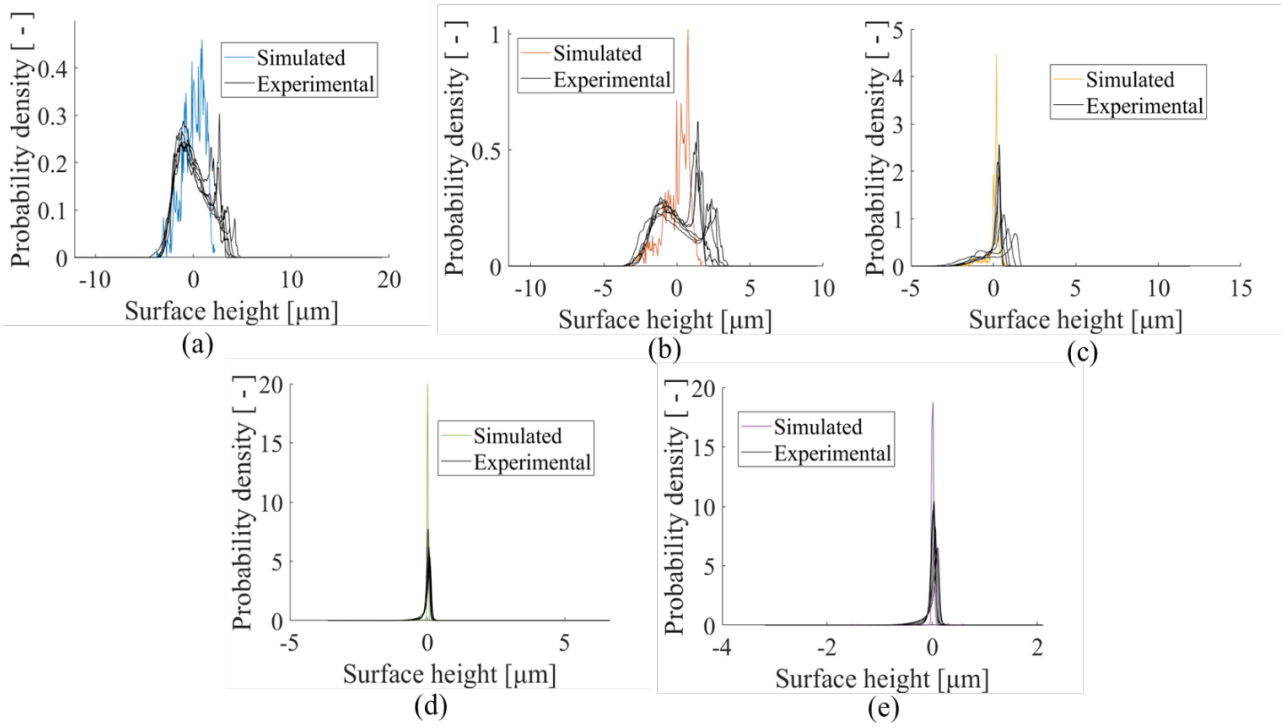

Fig. 9. Surface height distributions for simulated polycrystal and real asperity flattening for compression tests of 11 mm DC04 disks with nominal punch pressure of (a) 50 MPa, (b) 150 MPa, (c) 300 MPa, (d) 450 MPa, and (e) 600 MPa.

Contact Area Ratio Measurements.

Approximations of contact area ratio for the compression experiments are plotted along with contact area ratio derived from simulation variables for the flattening simulation in Figure 10. Because of the significant impact that choosing bins for the height data has, for comparison, bin counts of 50, 200, and 400 were used for the approximately 2 million points in the scans. The simulated data shows a close to linear increase in contact area with increasing pressure up to the point where subsurface strain begins and starts to accelerate the rate of contact area increase. As more of the surface is in contact, the formation of new contact area gradually slows and finally reaches full contact. The experimental data follows a somewhat different trend. The 50 MPa condition has an artificially high estimated contact area ratio, due to the mode height sometimes corresponding to the bottom of the valleys on the surface rather than the top of the peaks. The wider spread of height values also means that

increasing bin count does not significantly affect the calculated contact area ratio for the 50 MPa condition. The calculated contact ratio decreases as the surface is flattened more at 150 MPa, then following a gradual increase up to 450 MPa, after which contact ratio remains approximately the same for the 600 MPa condition. While the estimated contact area is much lower for the experiments than the corresponding simulations, both exhibit a leveling off of contact area around 450 MPa nominal pressure.

The possible reasons for wider peaks on the height distributions discussed in the previous subsection would also contribute to an undercounting of contact and could contribute to this gap. Especially at higher pressures when the peaks begin to become more symmetrical, there are likely many data points on the surface at a height below the mode which were also participating in contact but not counted. For the most extreme case of a perfectly symmetrical peak, this would be an undercounting of contact area ratio by 50%. A further point of note is the difference between the results when the number of bins used to create the height distribution is changed. Generally, increasing the bin count decreases the calculated value for contact ratio, however there is not an indication that more bins are strictly more accurate; while the resolution of the height distribution increases with bin count, the number of points in each bin decreases, introducing another source of uncertainty. This is supported by the fact that the standard deviation does not strictly increase or decrease for all the data points with bin size.

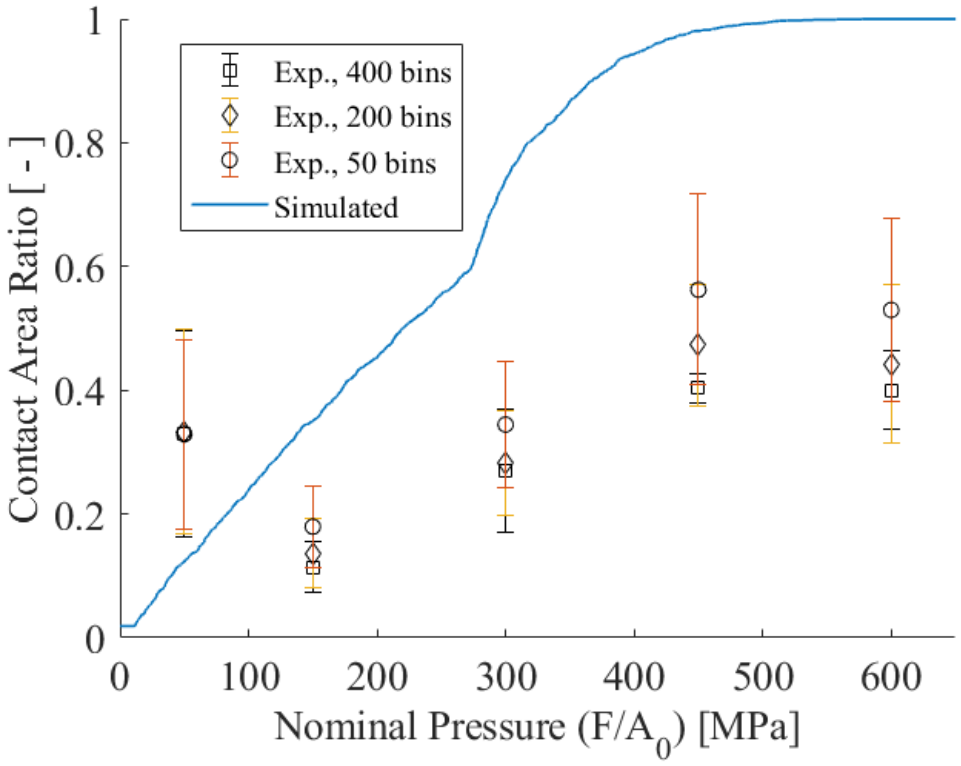

Fig. 10. Plot of contact area ratio as a function of nominal contact pressure for experimental and simulated polycrystal compression tests of 11 mm DC04 steel disks. Markers are mean values and error bars show one standard deviation. Real contact area is approximated for the experimental case via a numerical probability density function created using either 50, 200, or 400 bins to approximate probability density values.

A comparison between the results of flattening simulations with a polycrystal submodel and a submodel with the same topography and homogenous material properties is shown in Figure 11. For the phase before bulk deformation begins, the behavior is essentially identical. Once subsurface bulk deformation starts, minimal differences between the models can be observed. When force increases, the two curves converge again. These results suggest that this modeling approach for flattening was validated while adding the possibility to model roughening, which does not exist with a continuum model.

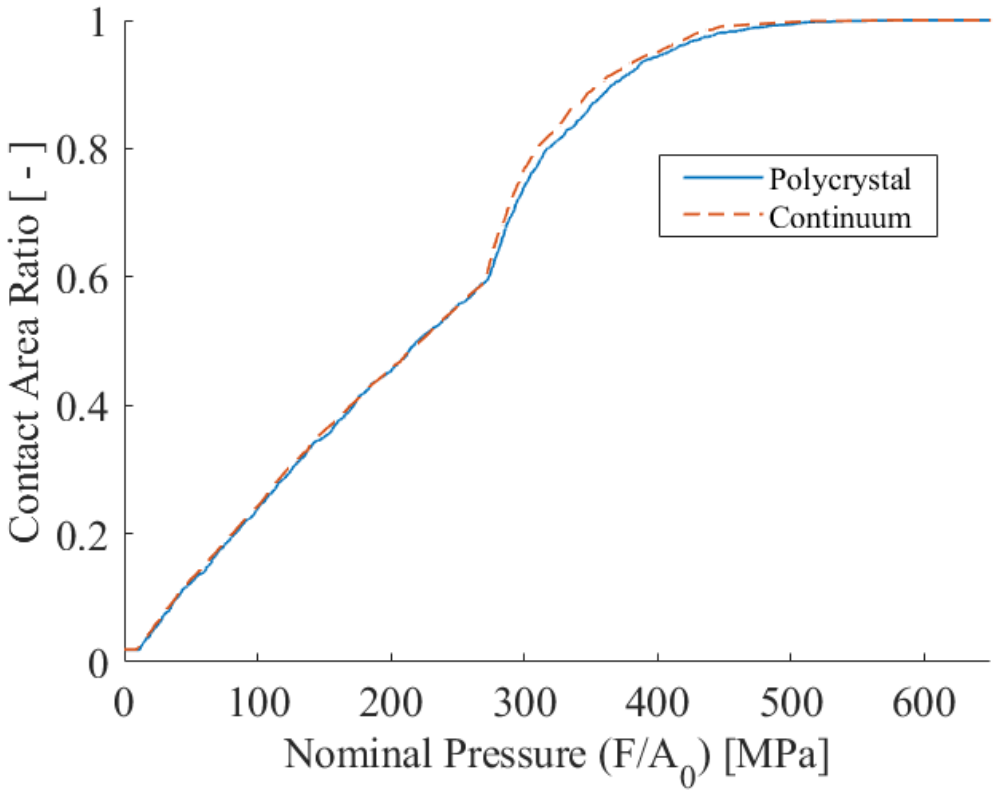

Fig. 11. Comparison of the evolution of contact area ratio with increasing nominal punch pressure between a model using a polycrystal tessellation where individual grain behavior is considered and a continuum model with uniform material properties.

Conclusion

Based on the results discussed above, the following conclusions are drawn:

- A crystal plasticity material model can predict asperity flattening comparable to that of a typical continuum material model. The use of a crystal plasticity model does not add significant insights to this simple case, but the ability to match the results of a continuum model suggests that a crystal plasticity model could be used to investigate cases with lower contact pressures and higher subsurface strains where roughening due to differential grain deformation becomes a critical surface phenomenon.
- Radial strain from compression increases the rate at which surface asperities flatten. However, the low level of this strain means that the roughening of the sheet surface, and preferential hardening of some grains over others predicted by crystal plasticity make negligible contributions to the surface evolution.
- Surface flattening, as characterized by height distributions and height maps, can be predicted with reasonable accuracy via finite element simulations. However, the challenges of experimental contact area ratio measurement make it difficult to assess how well real contact area evolution can be predicted.

Acknowledgement

The authors would like to thank the Independent Research Fund Denmark (grant ID 10.46540/3105-00169B) for funding of this research. The authors would also like to thank Tata Steel Europe for providing the DC04 sheet used in this study.

References

[1] E. Orowan, The Calculation of Roll Pressure in Hot and Cold Flat Rolling, Proc. Inst. Mech. Eng., 150 (1943) 140-167.

[2] M. C. Shaw, A. Ber, and P. A. Mamin, Friction Characteristics of Sliding Surfaces Undergoing Subsurface Plastic Flow, J. Basic Eng., 82 (1960) 342–345.

[3] T. Wanheim, Friction at high normal pressures, Wear, 25 (1973) 225–244.

[4] T. Wanheim, N. Bay, and A. S. Petersen, A theoretically determined model for friction in metal working processes, Wear, 28 (1974) 251–258.

[5] M. P. F. Sutcliffe, Surface asperity deformation in metal forming processes, Int. J. Mech. Sci. 30 (1988) 847–868.

[6] H. Ike and A. Makinouchi, Effect of lateral tension and compression on plane strain flattening processes of surface asperities lying over a plastically deformable bulk, Wear 140(1990)17-38.

[7] Z.G. Wang, Y. Yoshikawa, T. Suzuki, and K. Osakada, Determination of friction law in dry metal forming with DLC coated tool, CIRP Ann. 63 (2014) 277–280.

[8] C.V. Nielsen, P.A.F. Martins, and N. Bay, Modelling of real area of contact between tool and workpiece in metal forming processes including the influence of subsurface deformation, CIRP Ann. 65 (2016) 261–264.

[9] J. Hol, M. V. Cid Alfaro, M. B. De Rooij, and T. Meinders, Advanced friction modeling for sheet metal forming, Wear, 286–287 (2012) 66–78.

[10] M. Shisode, J. Hazrati, T. Mishra, M. De Rooij, and T. Van Den Boogaard, Evolution of real area of contact due to combined normal load and sub-surface straining in sheet metal, Friction 9 (2021) 840–855.

[11] M. Zwicker, N. Bay, and C. V. Nielsen, A discussion of model asperities as a method to study friction in metal forming, Discov. Mech. Eng. 2 (2023) 3.

[12] P. K. Saha and W. R. D. Wilson, Influence of plastic strain on friction in sheet metal forming, Wear 172 (1994) 167–173.

[13] O. Zinovieva, V. Romanova, R. Balokhonov, A. Zinoviev, and Z. Kovalevskaya, Numerical Study of the Influence of Grain Size and Loading Conditions on the Deformation of a Polycrystalline Aluminum Alloy, J. Appl. Math. Phys. 2 (2014) Art. no. 6.

[14] A.V. Panin *et al.*, Mesoscopic surface folding in EK-181 steel polycrystals under uniaxial tension, Phys. Mesomech. 15 (2012) 94–103.

[15] Y. Wu, V. Recklin, and P. Groche, Strain Induced Surface Change in Sheet Metal Forming: Numerical Prediction, Influence on Friction and Tool Wear, J. Manuf. Mater. Process. 5 (2021) Art. no. 2.

[16] H. J. Bong and J. Lee, Crystal plasticity finite element–Marciniak-Kuczynski approach with surface roughening effect in predicting formability of ultra-thin ferritic stainless steel sheets, Int. J. Mech. Sci. 191 (2021) 106066.

[17] Y. Wu, V. Recklin, and P. Groche, Strain Induced Surface Change in Sheet Metal Forming: Numerical Prediction, Influence on Friction and Tool Wear, J. Manuf. Mater. Process. 5 (2021) Art. no. 2.

[18] Sensofar S Neox confocal microscope in DTU Metrology lab, used 2025. https://doi.org/10.57735/13866.

[19] M.P. Shisode, J. Hazrati, T. Mishra, M. B. de Rooij, and A. H. van den Boogaard, Semi-analytical contact model to determine the flattening behavior of coated sheets under normal load, Tribol. Int. 146 (2020) 106182.

[20] Metallic materials – Tensile testing – Part 1: Method of test at room temperature (ISO 6892-1: 2019) .

[21] R. Quey, P. R. Dawson, and F. Barbe, Large-scale 3D random polycrystals for the finite element method: Generation, meshing and remeshing, Comput. Methods Appl. Mech. Eng. 200 (2011) 1729–1745.

[22] D. Zhao, C. Xin, T. Jin, X. Yan, S. Ma, and Z. Wang, Evolution of face-centered-cubic polycrystalline plastic anisotropy under biaxial loading by crystal plasticity finite element method, Eng. Comput. 37 (2019) 895–908.

[23] A. Carley-Clopton, G. Winther, O. Mishin, and C. Nielsen, Multiscale simulation of surface roughening of a deep drawing steel due to subsurface plastic deformation, MATEC Web Conf. 408 IDDRG 2025 (2025).

[24] F. Roters *et al.*, DAMASK – The Düsseldorf Advanced Material Simulation Kit for modeling multi-physics crystal plasticity, thermal, and damage phenomena from the single crystal up to the component scale, Comput. Mater. Sci. 158 (2019) 420–478.

[25] M. Shisode, J. Hazrati, T. Mishra, M. De Rooij, and T. Van Den Boogaard, Evolution of real area of contact due to combined normal load and sub-surface straining in sheet metal, Friction, 9 (2021) 840–855.

[26] N. Bay and G. Gerved, Tool/workpiece interface stresses in simple upsetting, J. Mech. Work. Technol. 14 (1987) 263–282.